

Article

Temperature Structure Inversion of Mesoscale Eddies in the South China Sea Based on Deep Learning

Jidong Huo^{1,2}, Jungang Yang^{2,3,*} , Liting Geng^{4,5}, Guangliang Liu^{4,5}, Jie Zhang^{1,3}, Jichao Wang⁶ 
and Wei Cui^{2,3} 

- ¹ College of Oceanography and Space Informatics, China University of Petroleum (East China), Qingdao 266580, China
- ² Technology Innovation Center for Maritime Silk Road Marine Resources and Environment Networked Observation, Ministry of Natural Resources, Qingdao 266061, China
- ³ First Institute of Oceanography, Ministry of Natural Resources of China, Qingdao 266061, China
- ⁴ Key Laboratory of Computing Power Network and Information Security, Ministry of Education, Shandong Computer Science Center (National Supercomputer Center in Jinan), Qilu University of Technology (Shandong Academy of Sciences), Jinan 250000, China
- ⁵ Shandong Provincial Key Laboratory of Computer Networks, Shandong Fundamental Research Center for Computer Science, Jinan 250100, China
- ⁶ College of Science, China University of Petroleum, Qingdao 266580, China
- * Correspondence: yangjg@fio.org.cn

Abstract: Mesoscale eddies are common in global oceans, playing crucial roles in ocean dynamics, ocean circulation, and heat transport, and their vertical structures can affect the water layers from tens to thousands of meters. In this study, we integrated sea surface height and sea surface temperature data into deep learning methods to study the mesoscale eddy subsurface temperature structure and to explore the relationship between sea surface data and eddy subsurface layers. In this study, we introduce Dual_EddyNet, a deep learning algorithm designed to invert the subsurface temperature structure of mesoscale eddies. Using this algorithm, we explore the impact of the sea surface height and sea surface temperature on the subsurface temperature structure inversion of mesoscale eddies. Furthermore, we compare different data fusion strategies, namely single-stream neural networks and dual-stream neural networks, to validate the effectiveness of the dual-stream model. To capture the interrelations among surface data and integrate feature information across various dimensions, we introduce the Triplet Attention Mechanism. The experimental results demonstrate that the proposed Dual_EddyNet performs well in reconstructing the three-dimensional structure of mesoscale eddies in the South China Sea (within a depth of 1000 m), with an inversion accuracy of 91.44% for cyclonic eddies and 95.25% for anticyclonic eddies. This algorithm provides a new method for inverting the subsurface temperatures of mesoscale eddies, and can not only be directly deployed in systems, embedded in ship moving platforms, etc., but can also provide a data reference for assimilations and numerical simulations, demonstrating its rich application potential.

Keywords: mesoscale eddies; temperature structure; deep learning



Citation: Huo, J.; Yang, J.; Geng, L.; Liu, G.; Zhang, J.; Wang, J.; Cui, W. Temperature Structure Inversion of Mesoscale Eddies in the South China Sea Based on Deep Learning. *J. Mar. Sci. Eng.* **2024**, *12*, 723. <https://doi.org/10.3390/jmse12050723>

Academic Editor: Eugen Rusu

Received: 4 March 2024

Revised: 12 April 2024

Accepted: 23 April 2024

Published: 27 April 2024



Copyright: © 2024 by the authors. Licensee MDPI, Basel, Switzerland. This article is an open access article distributed under the terms and conditions of the Creative Commons Attribution (CC BY) license (<https://creativecommons.org/licenses/by/4.0/>).

1. Introduction

The South China Sea is a vital marginal sea in the Pacific region, holding significant geographical importance. Mesoscale eddies, a common oceanic phenomenon, play a crucial role in heat transfer and nutrient transport in the South China Sea [1]. Typically, mesoscale eddies can survive for several days or even years, with spatial scales ranging from tens to hundreds of kilometers. In the vertical dimension, they exhibit nonlinear and isolated features, with their influence extending to depths of several kilometers [2]. Based on their rotational direction and vorticity, mesoscale eddies can be categorized as cyclonic eddies (CEs) or anticyclonic eddies (AEs) [3,4]. In the northern hemisphere, cyclonic

eddies, also known as cold-core eddies, transport cold water from the lower to the upper layers, resulting in lower temperatures within the eddy. Anticyclonic eddies, on the other hand, transport warm water from the upper layers to the lower layers, causing higher temperatures within the eddy compared to the surrounding ocean [5]. Mesoscale eddies contain a significant portion of the kinetic energy of overall ocean circulation, accounting for 80% to 90% or more [6]. Their motion generates upwelling, transporting nutrients from the ocean's subsurface to the thermocline, which is indispensable for transferring nutrients, organic salts, heat, and energy [7]. Mesoscale eddies influence parameters such as the sea surface temperature (SST), sea surface salinity (SSS), and sea surface height (SSH) in upper ocean layers, consequently affecting ocean circulation and ecosystems [8]. They lead to anomalies in sea surface temperature, altering turbulent heat flux, sea surface wind speed, divergence, cloud cover, and precipitation and thereby giving rise to distinct three-dimensional spatial structures. Mixing at mesoscale eddy fronts and its effect on the advection of particles impact the ocean chemistry and biological environment in local areas, which has significant implications for fisheries, military operations, and the marine ecosystem. Therefore, the study of mesoscale eddies, particularly their subsurface aspects, should not be overlooked.

In recent years, high-resolution remote sensing data have rapidly evolved, becoming essential in various fields such as oceanography and meteorology. However, by relying solely on remote sensing data, only surface-level analyses can be performed, failing to directly detect information within the ocean. Compared to remote sensing observations, in situ oceanographic data, such as Argo data, offer insight into the sea's subsurface profiles. Several researchers have conducted studies on subsurface structure inversion. For instance, Hu et al. [9] analyzed a cyclonic eddy near the Vietnamese coast using extensive CTD observational data, examining its three-dimensional structure from the sea surface to a depth of 500 m, and found that the axis of the eddy tilts southwestward with depth. Dong et al. [10] utilized a regional ocean model (ROMS) to analyze mesoscale eddies in the Southern California Bight, defining three shapes of eddies: bowls, convex lenses, and cones. Jeong et al. [11] estimated the ocean subsurface temperature (OST) using a multivariate linear regression model and analyzed the characteristics of global sea surface temperature anomalies (SSTAs) and mixed layer depths. Ali et al. [12,13] employed a back propagation (BP) neural network method combined with satellite observational data from the Arabian Sea system, such as SST, SSH, wind stress, net radiation, and heat flux data, to estimate ocean temperature profiles. Su et al. [14,15] proposed using a support vector machine method and satellite sea surface observational data to estimate subsurface temperature anomalies (STAs) for over 1000 m in the Indian Ocean. They subsequently used Argo and satellite sea surface data to estimate the ocean temperature structure through a random forest (RF) approach. Han et al. [16] introduced a convolutional neural network that integrates multiple surface parameters, including the SST, SSH, and SSS, to construct monthly Pacific subsurface temperature structures, improving the subsurface temperature structure inversion accuracy. Cosne et al. [17] used unsupervised methods to investigate local ocean currents in the North Atlantic Ocean, characterizing local regression relationships between the sea surface temperature, sea surface anomalies, and vertical temperature fields. Chen et al. [18] proposed an improved deep neural network that estimates the vertical profile of the chlorophyll-a concentration using multilayer perceptron and Gaussian activation functions, achieving inversion from surface ocean data to the subsurface. Yu et al. [19] introduced the ECN convolutional neural network algorithm to invert the temperature structure of mesoscale eddies in the northwest Pacific Ocean, achieving accuracy rates of 89.64% for cyclonic eddies and 87.25% for anticyclonic eddies. Xie et al. [20] proposed an Attention U-net model to establish a subsurface salinity field in the South China Sea based on satellite data and Copernicus reanalysis data.

Overall, in situ ocean data such as Argo are often used in ocean subsurface studies, but they encounter problems related to uneven spatiotemporal distributions, discontinuities, and low spatial resolutions, and do not fully meet the requirements for understanding the

internal dynamics of mesoscale eddies [21,22]. Dynamic methods mainly rely on numerical simulations, dynamic models, and other forms to construct three-dimensional mesoscale eddy structures, which have certain drawbacks such as requiring significant computational resources and depending on expert experience [23,24]. While numerical simulations like ROMSs have certain advantages, data assimilation models are susceptible to initialization and uncertainty factors. Additionally, these models can be complex and computationally intensive. Existing statistical methods do not fully leverage the features of ocean surface data; they often are limited, only use single features, and exhibit relatively poor nonlinear fitting capabilities. Consequently, they fail to fully harness the data, leaving significant room for improvements in accuracy [21]. Deep learning possesses certain advantages. It allows for the separation of training and inference stages, rendering it more convenient for application on edge platforms with limited computational power. Additionally, it can flexibly analyze small regions without the need for boundary conditions. Moreover, deep learning requires fewer computational resources and facilitates easy transfer learning with new data, eliminating the need for re-simulation. Deep learning technology has been widely used in oceanography and has made some progress, such as in the inversion of oceanic subsurface structures [25]. However, the study of the three-dimensional morphology of mesoscale eddies remains a challenge due to their susceptibility to factors such as the topography, their more complex physical characteristics, and the need for more detailed spatial observational data [26].

Based on the above issues, in this article, a dataset is constructed for the inversion of mesoscale eddy subsurface structures based on Copernicus reanalysis data. Recognizing the complex dynamic processes and nonlinear characteristics within mesoscale eddies [27,28], we propose a deep learning approach that integrates SSH and SST data to achieve the inversion of the three-dimensional temperature structure of mesoscale eddies. The algorithm presented in this study was used to investigate the impact of the SST and SSH on the inversion of the subsurface temperature structure of mesoscale eddies. Furthermore, we explored different data fusion strategies, including single-stream neural networks and dual-stream neural networks, validating the effectiveness of the dual-stream model. To fully exploit the value of the data, we introduced the Triplet attention mechanism to enhance the inversion accuracy and integrated feature information from different input dimensions. The proposed algorithm successfully reconstructed the three-dimensional temperature structure of the mesoscale eddies in the South China Sea (within a depth of 1000 m). The accuracy of cyclonic eddy inversion reached 91.44% in experiments, while the anticyclonic eddy inversion accuracy reached 95.25%. This study opens up a new perspective using artificial intelligence. Unlike numerical simulation methods, this algorithm has advantages such as a fast speed and low computational power consumption. If trained well enough, it can even surpass traditional methods. In this study, the Dual-EddyNet algorithm is proposed as a deep learning technique to enable data-driven inversion of the subsurface temperature of mesoscale eddies. This algorithm can quickly obtain subsurface temperature information using input sea surface parameters without the need for manual intervention. This method can be used as a standalone tool to predict the temperature of the subsurface layer of mesoscale eddies in the South China Sea in systems such as moving shipping platforms, ocean detection devices, ocean monitoring systems, etc. Deep learning methodologies can additionally provide initialization data for traditional numerical simulations and similar approaches. With sufficiently refined training, the deep learning model may even surpass and supplant conventional assimilation and numerical simulation techniques. Therefore, this algorithm has good application potential. The main contributions of this research include:

- (1) We construct a dataset for the inversion of the subsurface temperature structure of mesoscale eddies by combining SSH, SST, and subsurface temperature reanalysis data. This dataset offers practical support, particularly for studying mesoscale eddies in the South China Sea.

- (2) Using a data-driven approach and deep learning technology, we build a network (Dual_EddyNet) that establishes the relationships between the sea surface and subsurface, incorporating multiple sources of sea surface data. As a result, we reconstruct the three-dimensional temperature field of mesoscale eddies within a depth of 1000 m in the South China Sea, significantly improving the inversion accuracy.
- (3) Based on the proposed Dual_EddyNet method, we investigate the trends in the three-dimensional temperature fields at different depths for cyclonic and anticyclonic mesoscale eddies in the South China Sea, with a focus on the impact of the SST and SSH.

2. Data and Data Preprocessing

2.1. Data

Sea surface height, sea surface temperature, and temperature profile data were used in this study to construct a three-dimensional temperature field dataset for the South China Sea (0–30° N, 105–130° E), with a horizontal resolution of 0.25° × 0.25° and a vertical depth range of 0–1000 m, comprising a total of 36 layers. The mesoscale eddy identification information used here was taken from Archiving Validation and Interpolation of Satellite Oceanographic (AVISO) (<https://www.aviso.altimetry.fr/en/home.html>, accessed on 22 April 2024) and the altimetric Mesoscale Eddy Trajectory Atlas product (META3.2 DT [29], <https://www.aviso.altimetry.fr/en/data/products/value-added-products/global-mesoscale-eddy-trajectory-product.html>, accessed on 22 April 2024). This dataset includes the latitude, longitude, radius, and amplitude of mesoscale eddies, updated from 1993 to the present, with a spatial resolution of 0.25° × 0.25° and a daily temporal resolution. This dataset can identify eddies with diameters ranging from 100 to 300 km, and the identification method is based on Absolute Dynamic Topography (ADT).

The sea surface parameters used in this study include the SSH and SST, sourced from the Copernicus Marine Data Store website (<https://resources.marine.copernicus.eu>, accessed on 22 April 2024), which is part of the Copernicus Marine Environment Monitoring Service (CMEMS). The data product is Global Ocean Physics Reanalysis with data ID GLOBAL_MULTIYEAR_PHY_001_030 from CMEMS global ocean eddy resolving. The spatial resolution is 0.083° × 0.083° with a daily temporal resolution, covering the period from 1993 to 2020.

Currently, in the inversion of the subsurface structure of mesoscale eddies, profile data are typically based on Argo data [30,31]. However, there are issues with low spatial resolutions, sparse data coverage, and a lack of continuity. This study used reanalysis data as a substitute for Argo data to address this issue. The Global Ocean Physics Reanalysis data product includes ocean profile temperature data. In this experiment, the subsurface temperature profiles of the mesoscale eddies were taken from this dataset, which consists of 75 vertical levels with a vertical depth of up to 1000 m. In this study, the first 36 layers of data were selected. The data information used in this study is presented in Table 1.

Table 1. Data description.

Dataset	Source	Variable	Temporal Resolution	Spatial Resolution	Time Period
META 3.2 DT	AVISO	latitude, longitude, time amplitude	Daily	0.25° × 0.25°	1 January 1993–9 February 2022
Reanalysis data	Copernicus	SSH, SST, temperature profile	Daily	0.083° × 0.083°	1 January 1993–26 December 2023

2.2. Data Preprocessing

Critical information, including the coordinates, radius, and time of the eddy center, was extracted from the mesoscale eddy dataset provided by AVISO, and separate datasets

were constructed for cyclonic and anticyclonic eddies. A relationship mapping was established based on the eddy center coordinates, time, sea surface data, and subsurface profiles. Subsequently, the mesoscale eddy subsurface temperature samples were divided based on temperature profile information to form a comprehensive sample library.

The process of constructing this sample library is shown in Figure 1; the specific steps are as follows:

- (a) The South China Sea region (0–30° N, 105–130° E) is selected. Critical information, such as the coordinates and time of the eddy center, is extracted from the AVISO mesoscale eddy dataset and separate cyclonic and anticyclonic eddy datasets.
- (b) The corresponding sea surface position coordinates are identified based on the eddy center coordinates and time. A 4×4 matrix is defined with the coordinates as the center, and sea surface information (SSH and SST) is extracted from the Copernicus reanalysis data within the specified region, establishing the relationship mapping between mesoscale eddies and the sea surface.
- (c) Subsurface temperature profile information is obtained within the corresponding region from the Copernicus reanalysis data. We select the first 36 layers of data (0–1000 m) as the ground truth data.

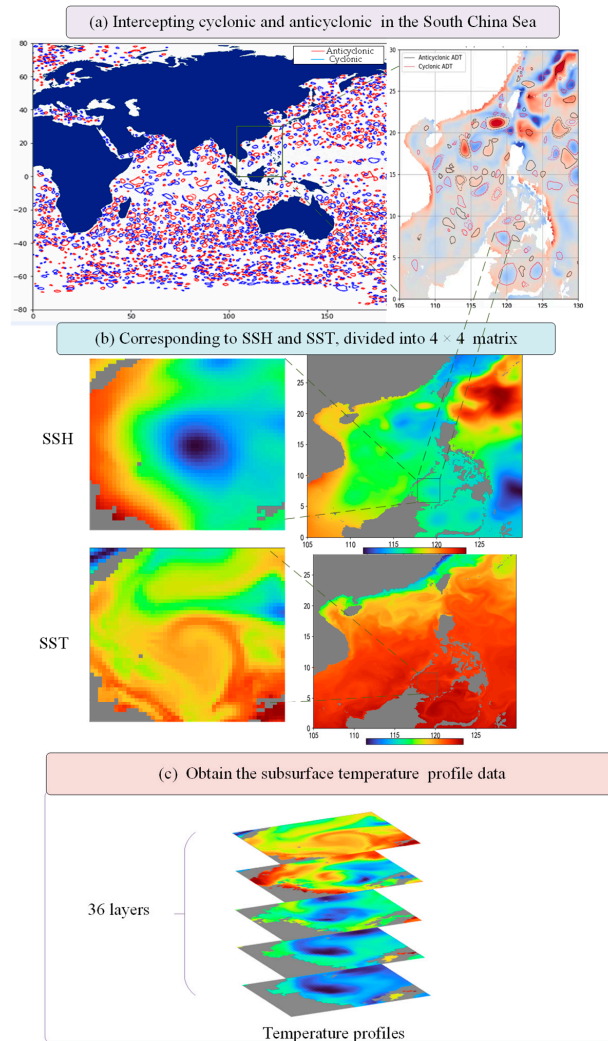


Figure 1. In the data processing flowchart, Meta 3.2 dt data are cropped to extract mesoscale eddy information in the South China Sea region. This involves partitioning a 4×4 matrix based on aligning key criteria such as time and eddy core coordinates with sea surface parameters and subsurface temperature profiles.

During this process, it is necessary to ensure the spatiotemporal consistency of the two sets of data. The two datasets are divided into the same grid system and processed at a unified resolution. The data are preprocessed using linear interpolation to achieve a uniform resolution of $0.25^\circ \times 0.25^\circ$. At the same time, in order to ensure that the two datasets are obtained from the same eddy, filtering is also performed. Using the automatic eddy current detection algorithm (py-eddy-tracker, PET), all vortices in Copernicus reanalysis data are simply partitioned and cyclonic and anticyclonic eddies are classified. Simultaneously, a threshold of 1° is set to filter out all vortices from the two datasets whose eddy deviation does not exceed this threshold. Ultimately, separate three-dimensional temperature inversion datasets for cyclonic and anticyclonic eddies are constructed. Figure 1 illustrates the data processing flowchart.

In this study, we focus on mesoscale oceanic eddies of the South China Sea during the five-year period from 2016 to 2020. The data were collected daily, and they consist of 146,630 cyclonic samples and 154,715 anticyclonic samples. The training data consist of 88,495 cyclonic samples and 92,754 anticyclonic samples from 2016 to 2018. The validation set consists of 29,174 cyclonic validation samples and 30,275 anticyclonic validation samples from 2019. The test set consists of 28,961 cyclonic test samples and 31,686 anticyclonic test samples from 2020.

3. Method

3.1. Convolutional Neural Networks

Convolutional neural networks (CNNs) use convolutional operations to extract features, map data to a high-dimensional feature space, and achieve feature regression [32,33]. They usually consist of convolutional layers, pooling layers, and fully connected layers. Convolution, as an important component, utilizes convolution operations to achieve feature extraction. The convolutional layer utilizes multiple different convolutional kernels to slide the receiver field, and a sliding window performs local calculations on the input data. Through weight sharing and local connection operations, the model's parameter count is reduced and its generalization ability is improved. All local connections of each filter in weight sharing use the same parameters, which can greatly reduce the network parameters and is suitable for sharing duplicate features. Additionally, it has a high processing efficiency for high-dimensional data and can automatically extract some advanced features, reducing the time for feature engineering. Shallow neural networks will acquire more local and general features, and as the network deepens, they will acquire deeper and more concrete features [34]. In this study, we use convolutional neural networks to construct a model in order to capture the temperature characteristics of the subsurface layer.

The U-net network [35], as shown in Figure 2a, is a mainstream convolutional neural network and has received widespread attention in fields such as semantic segmentation. This model includes an encoding and a decoding stage. The encoding stage is mainly used for backbone feature extraction, utilizing convolutional layer stacking to effectively obtain deep information. In the decoding stage, feature extraction is strengthened, and the features obtained in the encoding stage are fused to combine the effective information from both stages. The U-net network has been widely used in the field of remote sensing due to its simplicity and efficiency. Xie et al. [20] and Liu et al. [36] have both adopted this convolutional network in the field of ocean remote sensing, verifying its effectiveness. However, the U-net Attention method proposed by Xie et al. was not targeted at mesoscale eddies; they constructed an ocean model to generalize and estimate mesoscale eddies, losing a certain degree of robustness. The attention mechanism used here is the CBAM [37] method, as shown in Figure 2b, which takes into account the correlation and interaction between sea surface parameters.

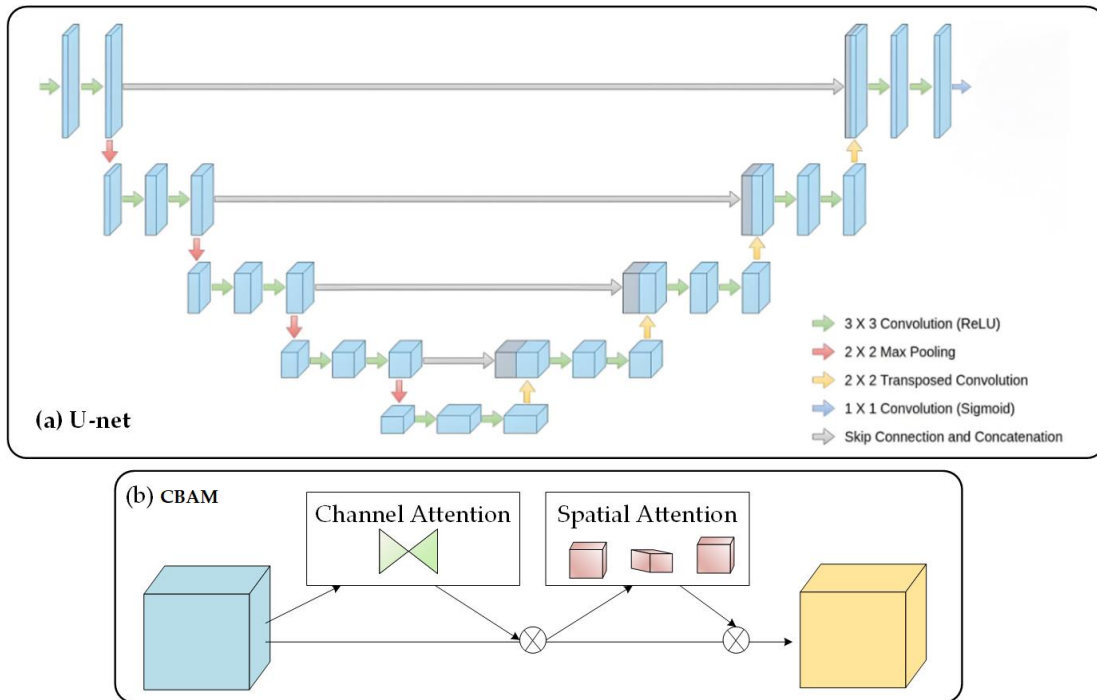


Figure 2. (a) is the model structure of U-net, and (b) is the structure of the CBAM attention mechanism.

3.2. The Overall Architecture of the Model

The method proposed in this study is a data-driven deep learning algorithm called Dual_EddyNet, based on an encoder–decoder structure, as shown in Figure 3a. It consists of two modules: an encoding stage for feature extraction of SSHs and SSTs and a decoding stage for feature fusion. The input data consist of two types of sea surface parameters: SSH and SST. During the inversion process, a 4×4 matrix with a resolution of $0.25^\circ \times 0.25^\circ$ is input, corresponding to a patch size of 17×17 points. Simultaneously, 36 layers of temperature profiles are employed as the ground truth for the inversion of the deep learning model at the depth level.

In the encoding stage, the dual-stream data of SST and SSH are input to explore the relationship between SST, SSH, and subsurface temperature. For feature extraction from SSH and SST, considering the complex nonlinear characteristics of mesoscale eddies, there is an inherent connection between SSH and SST. A data feature fusion network is constructed to capture this relationship between SSH and SST, and skip connections are utilized to reduce the risk of overfitting. In this process, the SSH and SST are separately input into the two branches of the neural network to model the subsurface temperature field. Feature extraction is performed within the same stream, and feature interaction is conducted between different streams to achieve data feature fusion.

The encoding stage deepens the network, and, thus, the feature maps become smaller to extract data at different resolutions. In the decoding stage, the feature outputs from each layer of the encoding stage are fused, and the solution is restored using deconvolution. To fuse feature information across different dimensions, the Triplet attention mechanism is incorporated into the model [38], as shown in Figure 3b, which utilizes a three-branch structure to combine channel attention and spatial attention, enabling cross-dimensional interactions and improving the model’s inversion accuracy. This can facilitate better interactions and capture potential features between data.

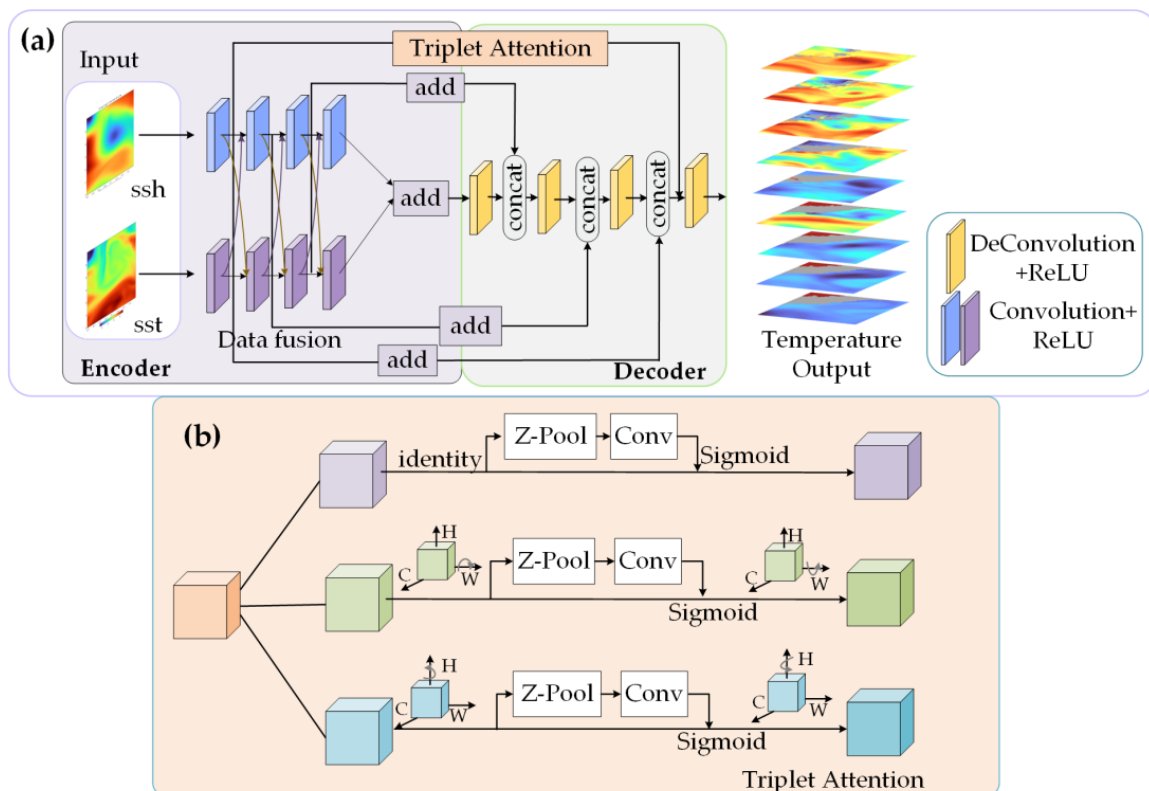


Figure 3. The architecture of the Dual_EddyNet model follows an encoder–decoder structure (a), primarily comprising a dual-stream input framework, a data fusion module, and a Triplet attention module (b).

3.3. Comparison of Single-Stream and Dual-Stream Models

The single-stream model, as shown in Figure 4a, adopts an encoder–decoder architecture. The encoding stage consists of four convolutional layers with ReLU activation functions, implementing down-sampling operations. The resolution decreases as the number of layers increases, and the feature maps become smaller, capturing deeper semantic information. In the decoding stage, deconvolution is used for up-sampling to restore the output resolution, making the feature maps larger. In this process, the input data are the fused SST and SSH data, with the subsurface temperature profile data as the ground truth. The model establishes the relationship between SSH, SST, and the subsurface temperature and uses surface data to invert the subsurface temperature.

The dual-stream model, as shown in Figure 4b, also adopts an encoder–decoder architecture. It differs from the single-stream model in that, in the encoding stage, SSH and SST data are input separately, and this allows for the construction of separate relationship models between the SSH and the subsurface temperature and between the SST and the subsurface temperature, allowing us to explore the impact of different sea surface parameters on three-dimensional structure inversion. Considering the complex nonlinear features of mesoscale eddies and the inherent connection between different sea surface parameters, a data fusion module is introduced to facilitate feature interaction between the SSH and SST. In the decoding stage, the dual-stream model achieves feature fusion, and skip connections are used within each layer to reduce the risk of overfitting while integrating features from the encoding stage.

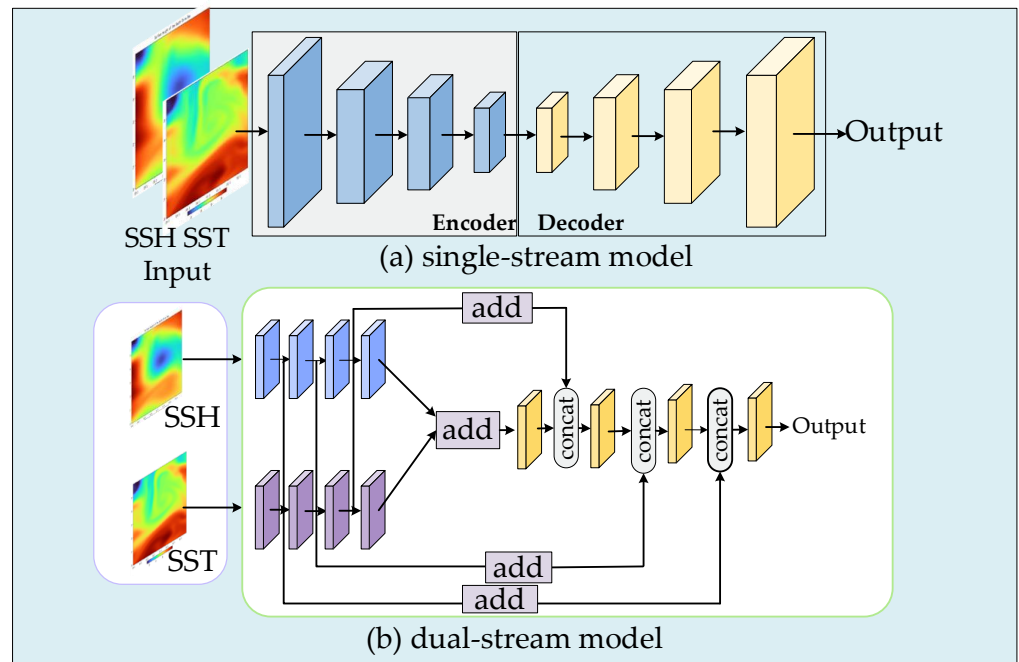


Figure 4. Architectures of single-stream and dual-stream models. (a) For the single-stream model structure, the data input is coupled. (b) For the dual-stream model structure, the input data are decoupled, and models of the relationship between SSH and the subsurface and the SST and the subsurface are established separately.

3.4. Triplet Attention

As a standalone U-Net network deepens, it can only acquire feature information at varying resolutions, thereby exhibiting a comparatively weaker capacity for capturing relationships between data. Therefore, in this study, Triplet attention is introduced to better capture the relationship between the input SSH and SST. In this approach, residual changes are used to establish inter-dimensional dependencies, facilitating effective aggregation of local key information.

Triplet attention is used here to study cross-dimensional interactions, as shown in Figure 5. \odot denotes broadcast element-wise multiplication and \oplus denotes broadcast element-wise addition. The fusion of channel and spatial attention is achieved by capturing the interaction between the spatial dimensions and the input tensor channel dimensions. The input tensor $X \in \mathbb{R}^{C \times H \times W}$ is passed to the three branches of the Triplet attention module. In the first branch, the identity residual branch structure is introduced. Z-Pool is initiated first, integrating the average and max pooling features to achieve dimension scaling. After a 7×7 convolution and batch normalization, attention weights are generated through the Sigmoid activation function and then multiplied by the identity residual branch’s output to obtain the first branch’s output. Here, Z-Pool is responsible for connecting this dimension’s max pooling and average pooling features, reducing the first dimensions of the tensor to two and thus retaining the rich features of the actual tensor while reducing its depth to reduce its weight. The formula for Z-Pool can be expressed as:

$$\text{Z-Pool}(x) = [\text{MaxPool}(x), \text{AvgPool}(x)] \tag{1}$$

In the second branch, the input tensor $X \in \mathbb{R}^{C \times H \times W}$ is rotated 90° counterclockwise along the W axis, resulting in a transformed tensor, denoted as $X \in \mathbb{R}^{W \times H \times C}$. After this, the Z-Pool operation is applied to achieve dimension scaling, resulting in an output represented as $X \in \mathbb{R}^{2 \times H \times C}$. Subsequently, the tensor passes through a 7×7 matrix and undergoes normalization to obtain the output denoted as $X \in \mathbb{R}^{1 \times H \times C}$. Attention weights

are generated using the Sigmoid activation function, and then the tensor is rotated 90° clockwise along the W axis, resulting in the output denoted as $X \in \mathbb{R}^{C \times H \times W}$.

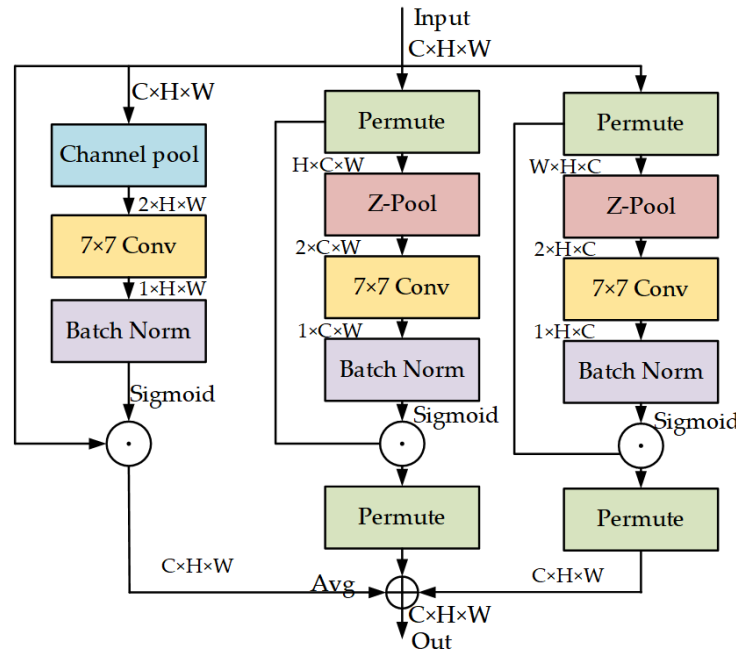


Figure 5. The Triplet attention module consists of three branches, establishing feature interactions between the H and W dimensions, the H and C dimensions, and the C and W dimensions.

Similarly, in the third branch, the input tensor is rotated along the H axis to establish feature interaction, resulting in an output denoted as $X \in \mathbb{R}^{C \times H \times W}$.

Finally, the outputs of the three branches are averaged and aggregated to obtain the final result.

4. Experiments

4.1. Evaluation Metrics

Experiments were conducted with a batch size of 64 and 50 epochs. The optimizer used in the experiments was Adam, and the learning rate was 1×10^{-3} . The loss function was SmoothL1 loss; the formula for the loss can be expressed as:

$$Loss = \begin{cases} \frac{1}{2}(y_i - \hat{y}_i)^2 / \text{beta}, & \text{if } |y_i - \hat{y}_i| < \text{beta} \\ |y_i - \hat{y}_i| - \frac{1}{2} * \text{beta}, & \text{otherwise} \end{cases} \quad (2)$$

where y_i is the target value, \hat{y}_i is the predicted value, and beta is the threshold, set to 1.0 by default.

The evaluation criteria for the experiments in this paper include R^2 , MAE, RMSE, and the explained variance score. R^2 measures the goodness of fit of the predicted data and takes a value between 0 and 1. A value closer to 1 indicates a better fit of the model to the data. The formula for R^2 can be defined as follows:

$$R^2 = \frac{\sum_i (y_i - \hat{y}_i)^2}{\sum_i (y_i - \bar{y}_i)^2}, \quad \bar{y}_i = \frac{\sum_{i=1}^n y_i}{n} \quad (3)$$

Here, n represents the number of samples, \hat{y}_i represents the predicted value, y_i represents the target value, and \bar{y}_i represents the average of the observed data.

The Mean Absolute Error (MAE) measures the sum of the absolute differences between the target and predicted variables. The MAE value ranges from 0 to positive infinity, with

a larger MAE value indicating a larger prediction error. The formula for the MAE can be expressed as:

$$MAE = \frac{\sum_i^n |y_i - \hat{y}_i|}{n} \tag{4}$$

Here, $| \cdot |$ denotes the absolute value and Σ denotes the summation.

The Root Mean Square Error (RMSE) can reflect the distribution of prediction errors; its formula is as follows:

$$RMSE = \sqrt{\frac{1}{n} \sum_{i=1}^n (y_i - \hat{y}_i)^2} \tag{5}$$

The explained variance score is a metric that measures the degree to which a model explains the variance in a dataset. It takes values between 0 and 1, with a value closer to 1 indicating better model performance. The formula can be expressed as:

$$\text{explain variance}(y_i, \hat{y}_i) = 1 - \frac{\text{var}\{y_i - \hat{y}_i\}}{\text{var}\{y_i\}} \tag{6}$$

where var represents the variance.

4.2. Experimental Results

4.2.1. Comparison of Input of Different Variables

In this study, input parameters were assessed and the model structure was validated using a single-stream approach. The subsurface temperature inversion for cyclonic and anticyclonic eddies were compared when only SSH data were used and when both SSH and SST data were used. Table 2 demonstrates that including the SST in addition to the SSH data enhances R^2 to differing extents for both cyclonic and anticyclonic cases. Specifically, for cyclonic eddies, there was a 0.09 increase in the R^2 , while for anticyclonic eddies, there was a 0.12 increase. The accuracy of cyclonic inversion and anticyclonic inversion increased by 8.4% and 4.34%, respectively. Additionally, the MAE values decreased by 1 °C for cyclonic eddies and 1.04 °C for anticyclonic eddies. The introduction of the SST has played a positive role in the retrieval of the sub-layer temperature of mesoscale eddies.

Table 2. Comparison of input of different variables.

Input	Model	R^2	MAE	Explained_Variance
SSH	Cyclonic	0.73	2.17	73.17%
SSH, SST	Cyclonic	0.82	1.17	81.57%
SSH	Anticyclonic	0.82	1.9	90.39%
SSH, SST	Anticyclonic	0.94	0.86	94.73%

4.2.2. Comparison of Different Model

The findings presented in this section provide further evidence to support the effectiveness of the proposed Dual_EddyNet. The subsurface temperature structure is inverted using the SSH and SST as inputs to compare the results obtained from both the single- and dual-stream models. According to Table 3, for cyclonic eddies, the dual-stream model exhibits a superior performance over the single-stream model, showing a reduction of 0.16 °C in the MAE and an increase of 0.07 in the R^2 , yielding an accuracy improvement of 8.93%. For anticyclonic eddies, the dual-stream model exhibits an enhancement compared to the single-stream model, indicating a decrease of 0.04 in the MAE and an increase in accuracy of 0.23%. These experimental findings prove that, for both cyclonic and anticyclonic eddy data, the dual-stream model outperforms the single-stream model.

Table 3. Comparison of single- and dual-stream models.

Input	Model	R ²	MAE	Explained Variance
Cyclonic	Single-stream	0.82	1.17	81.57%
Cyclonic	Dual-stream	0.89	1.01	90.50%
Anticyclonic	Single-stream	0.94	0.86	94.73%
Anticyclonic	Dual-stream	0.94	0.82	94.80%

4.2.3. Ablation Experiments

To better demonstrate the effectiveness of the algorithm proposed in this study, relevant ablation experiments were conducted for cyclonic and anticyclonic eddies. Firstly, for mesoscale cyclonic eddies, experiments were conducted using only the dual-stream model, followed by experiments incorporating the dual-stream model with the addition of the Triplet attention module and the addition of the data fusion module, as shown in Table 4, ✓ represents the method used. The results show that the introduction of Triplet attention in the dual-stream model is beneficial, with a decrease in the MAE of 0.04 °C and an increase in the explained variance score of 0.19%. Furthermore, after the introduction of the data fusion module, the ultimate proposed model (Dual_EddyNet) exhibited a decline in the MAE of 0.06 °C and an improvement in the explained variance score of 0.75% compared to the dual-stream model combined with the Triplet attention method. Compared to the dual model, the R² increased by 0.02, the MAE decreased by 0.42 °C, and the explained variance score increased by 0.94%. These results indicate that the introduction of the Triplet attention module and the data fusion module effectively enhances the performance of the dual-stream model.

Table 4. Ablation experiments for cyclonic eddies.

Dual Stream	Attention	Data Fusion	R ²	MAE	Explained Variance
✓			0.89	1.01	90.50%
✓	✓		0.89	0.97	90.69%
✓	✓	✓	0.91	0.59	91.44%

Similarly, the algorithm proposed in this study exhibited an improved performance in subsurface temperature inversion of anticyclonic eddies to varying degrees, as shown in Table 5, ✓ represents the method used. The method proposed in this study (Dual_EddyNet) achieved an R² of 0.95 in subsurface temperature inversion in anticyclonic eddies.

Table 5. Ablation experiments for anticyclonic eddies.

Dual Stream	Attention	Data Fusion	R ²	MAE	Explained Variance
✓			0.94	0.82	94.80%
✓	✓		0.94	0.79	94.96%
✓	✓	✓	0.95	0.57	95.25%

4.3. Results and Analyses

The inversion results for cyclonic eddies at depths of 0–1000 m can be seen in Figure 6, which includes R², RMSE, and MAE evaluation metrics. The inversion R² values are all greater than 0.5, indicating that the inversion results at each depth are within a relatively good accuracy range. The R² value reaches a peak at middle depths of 50–500 m and then falls off. R² is used to assess the fitting degree of the prediction results to the actual outcomes. The closer the predicted values are to the real values, the higher the R² value, indicating a better data fit. However, the correlation between the surface and deep data decreases as the depth increases. Shallow ocean data (50–500 m) exhibit a strong correlation with the surface data, while deep ocean data (500–1000 m) show a weaker correlation with surface data. Therefore, the R² value peaks at a depth of 50–500 m before decreasing.

Furthermore, because the South China Sea is a marginal sea, the adjacent land easily influences deep sea areas, decreasing the inversion accuracy. The other metrics, the RMSE and MAE, exhibit a consistent overall trend, showing an initial increase followed by a decrease. The changes in the shallow sea areas are significant, with relatively high errors, mainly due to the multitude of influencing factors in the sea surface layer, leading to more complex water movements.

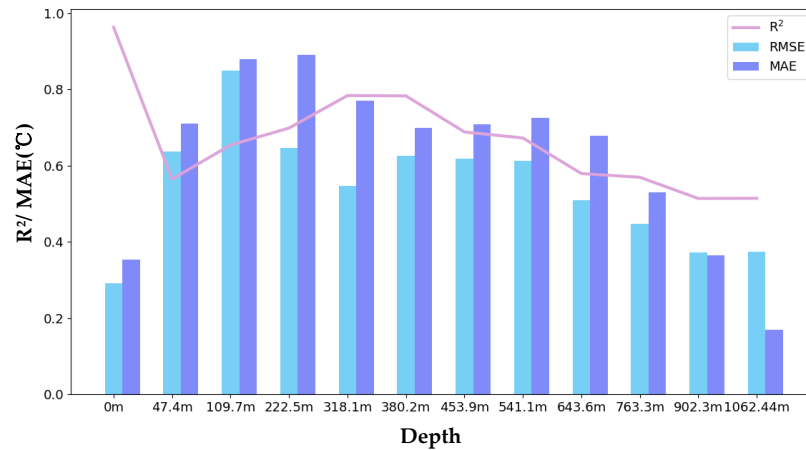


Figure 6. Inversion results of cyclonic eddies, including the R², MAE, and RMSE.

Figure 7 shows the accuracy map of the surface temperature data of mesoscale cyclonic eddies inverted using the Dual_EddyNet model, which presents the inversion results at different depths. The horizontal axis (predict) represents the predicted temperature values of cyclonic eddies inverted by Dual_EddyNet, while the vertical axis (target) represents the actual temperature values of the reanalysis data. The red line represents the regression line. The closer the scatter points are to the red line, the higher the inversion accuracy of Dual_EddyNet. The more aggregated the scatter points, the denser the scatter density, and the closer the color is to red. From the figure, most scatter points are within a reasonable error range.

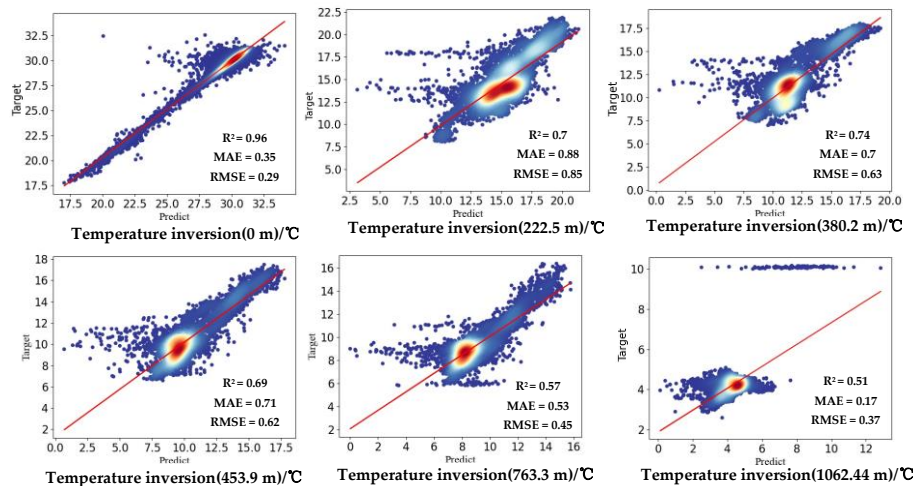


Figure 7. Inversion scatter map of cyclone eddies.

We investigated an anticyclonic case on 1 January 2020, with Figure 8 showing the mesoscale eddy subsurface temperature predicted by the proposed algorithm, Dual-EddyNet, as well as the true temperature from reanalysis data. This figure shows the eddy temperature state of the cyclonic eddy from 0 to 1000 m. It can be seen that, in cyclonic eddy inversion, the inversion of the sub surface layer of vortices in the 0–400 m range is

not very stable; for example, the inversion effect of the temperature at 109.7 m deteriorates to a certain degree. Corresponding to the eddy inversion diagram in Figure 6, the R^2 value also weakens at this layer. At the same time, it can be seen that the eddy is in a dissipating state at 380.2 m, and the predicted inversion effect has rebounded to a certain extent. As the depth increases, the correlation between deep temperature and surface data decreases, the inversion R^2 decreases, and the inversion effect also weakens.

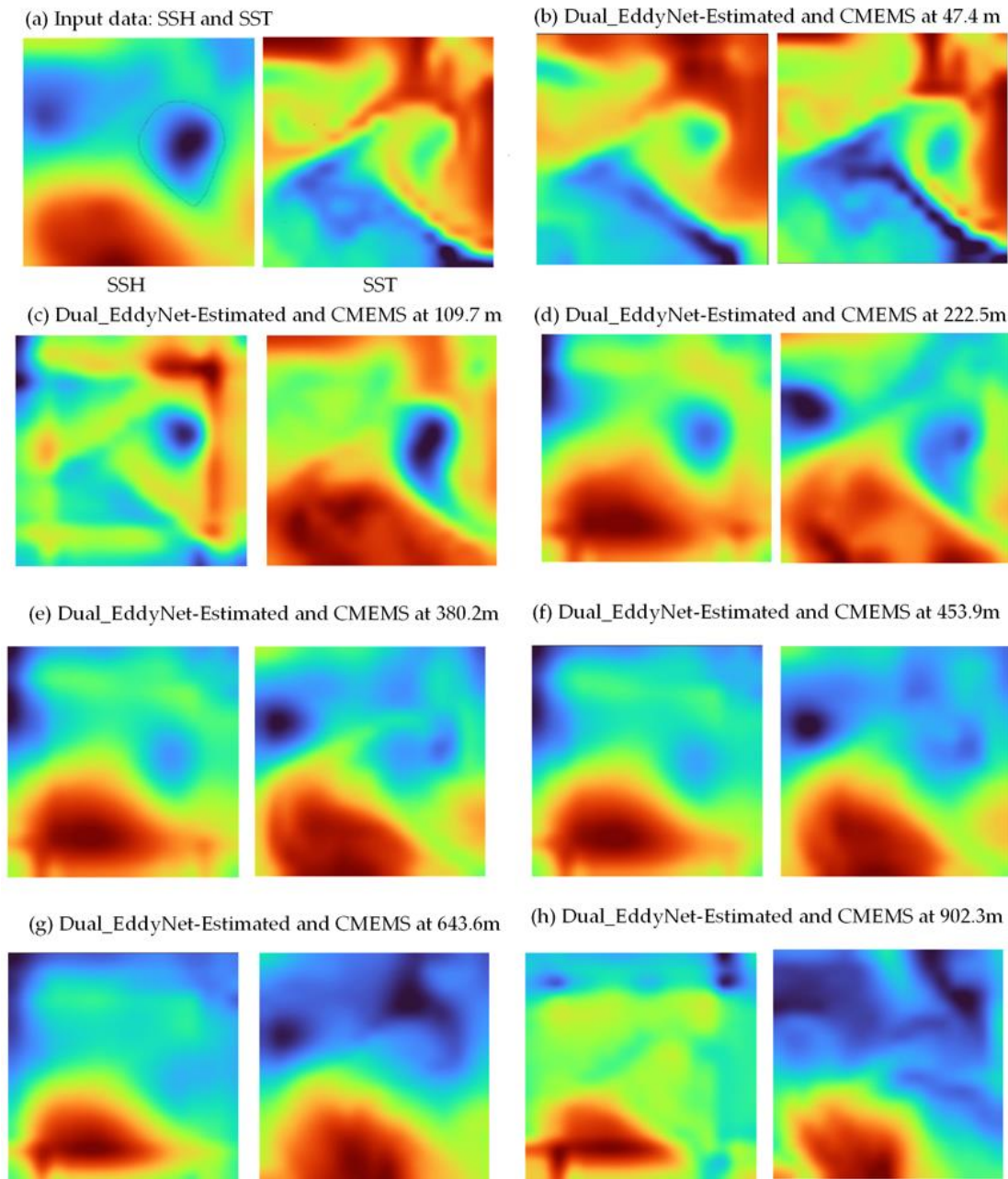


Figure 8. Comparison between the predicted and actual values of the cyclonic eddy (21.75° N, 128° E) on 1 January 2020. The left image in (a) shows the input data SSH, the right image shows the SST, and (b–h) show the visualization of the predicted and actual vortices at different depths. The left side shows the predicted performance of the Dual-EddyNet algorithm, and the right image shows the actual performance.

Figure 9 shows the inversion results for anticyclonic eddies at 0–1000-m depths, also showing the R^2 , RMSE, and MAE evaluation metrics. The inversion R^2 values are all greater than 0.5, indicating that the inversion results at each depth are within a relatively good accuracy range. However, at mid–shallow depths, the R^2 fluctuates significantly, exhibiting a concave shape, especially where there is a significant temperature change in the thermocline layer, resulting in a decrease in the R^2 and an increase in the RMSE, highlighting a noticeable decrease in the inversion performance. This is due to the complex nonlinear characteristics of mesoscale eddies in mid–shallow layers, which are highly susceptible to the influence of external factors such as tides, El Niño events, and wind fields. As the depth increases, the R^2 tends to decrease slowly, primarily because the complex dynamic processes in the deeper sea areas are poorly represented by the surface parameters. Consequently, the inversion performance is not ideal. Additionally, the influence of factors related to the marginal South China Sea leads to a more pronounced decrease in the R^2 in the deep sea areas. However, with an increasing depth, the RMSE and MAE decrease, the temperature fluctuation in deep-sea areas is minimal, resulting a reduction in the inversion error.

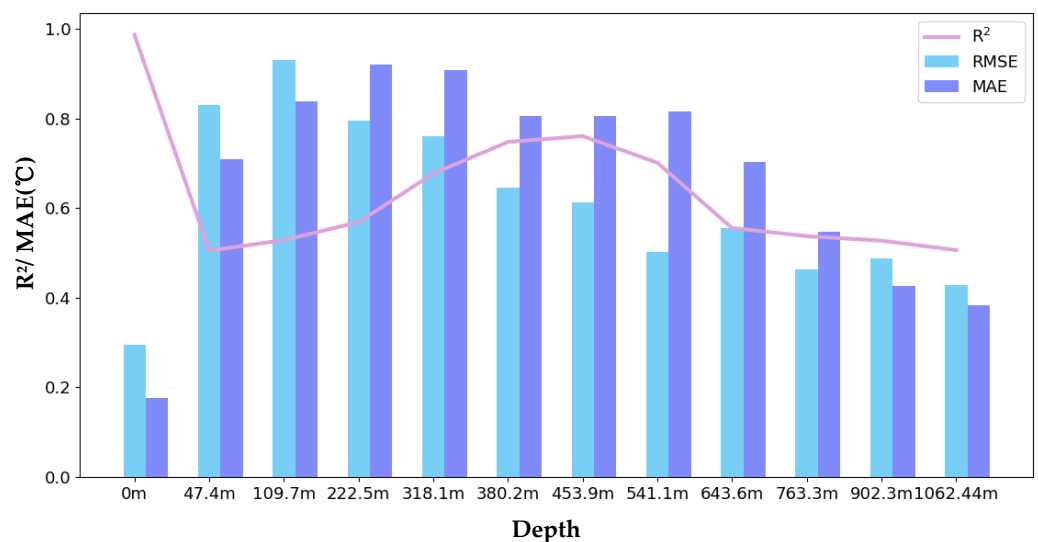


Figure 9. Inversion results of anticyclonic eddies, including the R^2 , MAE, and RMSE.

Overall, at depths of 0–1000 m, the model’s RMSE initially increases and then slowly decreases, while the R^2 shows initial decreases and then gradually grows, but exhibits a decreasing trend in deeper areas. These results indicate that as the depth increases, the model’s ability to fit the data deteriorates and its inversion capability weakens, especially in the marginal sea areas facing the South China Sea, where errors are more likely due to the influence of deep-sea topographical factors, making the inversion in deeper layers more complex.

In Figures 6 and 9, the R^2 , RMSE, and MAE exhibit similar trends. The RMSE and MAE do not exhibit significant temperature changes in shallow layers (50–100 m), so the RMSE at this stage is small. The correlation between the input sea surface data and the shallow sea temperature is high, so the R^2 is generally higher and the prediction effect is better. Due to the influence of other surface factors, there are significant changes in the middle and shallow layers, and the inversion effect first decreases and then increases. At higher depths, temperature fluctuations are relatively small, resulting in a lower RMSE. The correlation between sea surface data and deep surface temperature weakens, leading to a decrease in the R^2 .

Figure 10 shows a comparison of temperature visualizations using Dual_EddyNet prediction and reanalysis data, taking an anticyclonic eddy on 2 January 2020 as a case study. The left image in Figure 10a shows the input SSH, the right image shows the SST,

and Figure 10b–h show visualizations of the predicted and actual eddy currents at different depths. The left image displays the predictive performance of the Dual_EddyNet algorithm, and the right image shows the actual performance. The inversion effect of the shallow eddy in the figure is good. As the depth increases, the correlation between the input surface data (SSH and SST) and the deep surface temperature decreases, and the inversion effect also weakens.

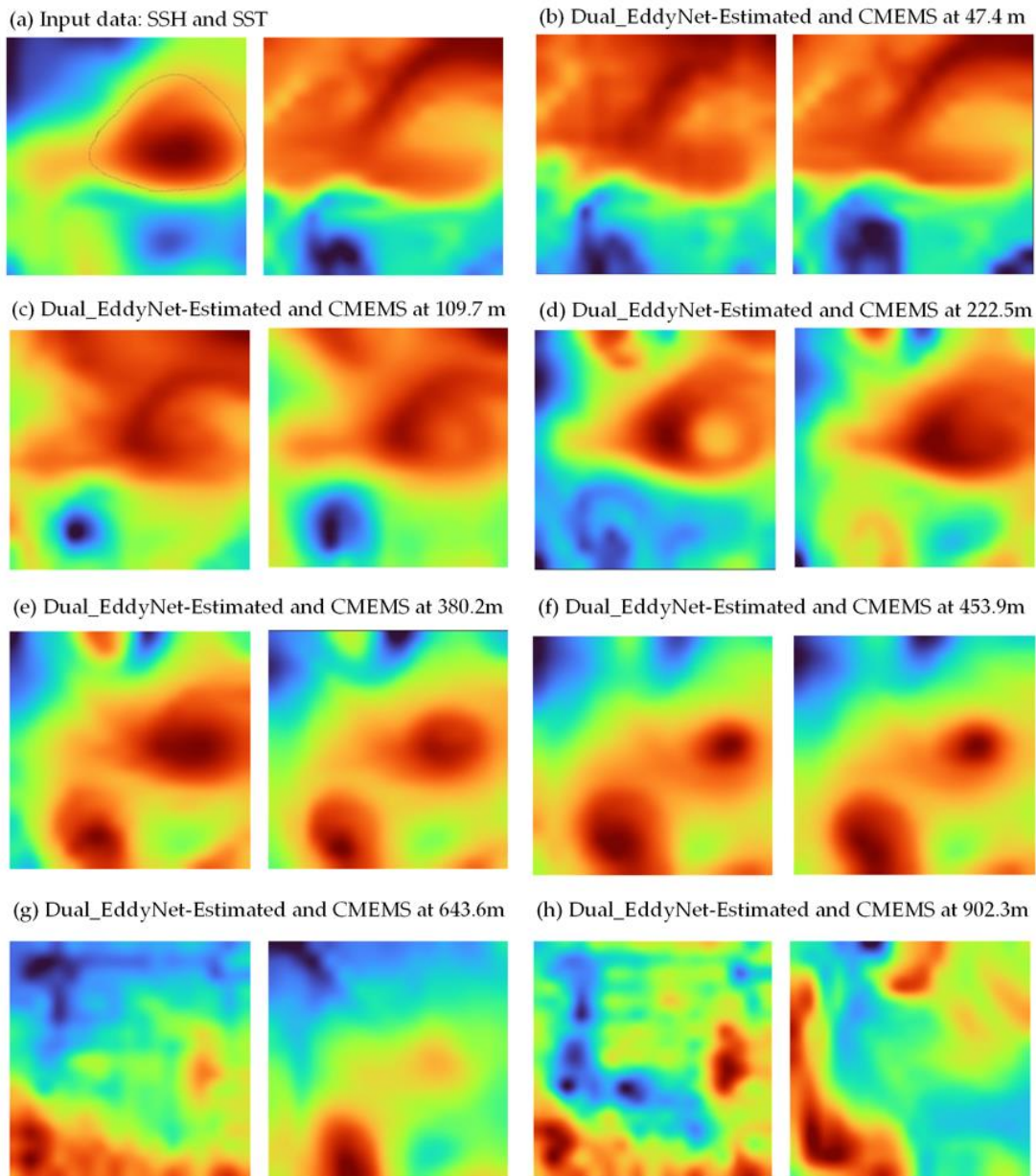


Figure 10. Comparison between the predicted and actual performance of the anticyclonic eddy (19.5° N, 125° E) on 2 January 2020.

Figure 11 presents a scatter plot of the inversion results for the surface temperature data of mesoscale anticyclonic eddies using the Dual_EddyNet model at different depths. The depths selected are 0 m, 222.5 m, 380.2 m, 453.9 m, 763.3 m, and 1062.4 m. Like the cyclonic eddy results, the model’s accuracy is influenced by the depth, with most scatter points falling within a reasonable error range.

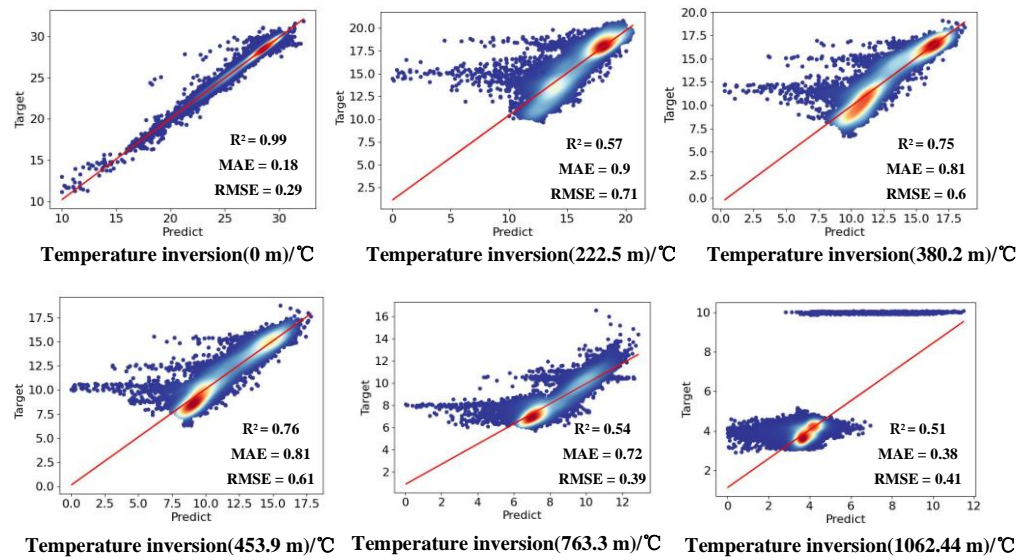


Figure 11. Inversion scatter map of anticyclonic eddies.

Furthermore, we compared the inversion capabilities of different models for mesoscale eddies in the South China Sea (studying 12 depth layers ranging from 0 to 1000 m), including the Dual_EddyNet proposed in this study (ours), U-net Attention (case 1) proposed by Xie et al. [20], and the U-net model (case 2), as shown in Figure 12. We compared the inversion results at different depths over 0–1000 m in 12 layers, and, as shown in the figure, our method achieved the best experimental results, which proves its effectiveness.

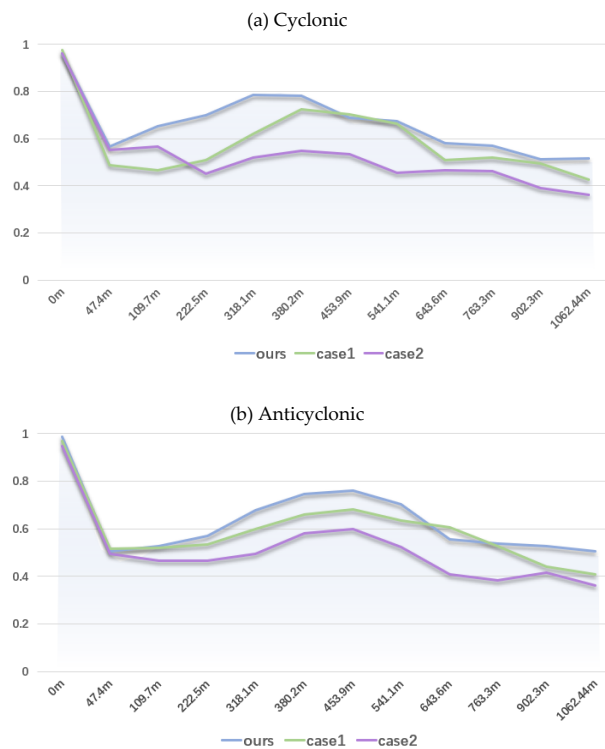


Figure 12. Comparison of the accuracy of our method and other algorithms. (a) Inversion results of different algorithms on cyclonic datasets; (b) inversion results of different algorithms on anticyclonic datasets.

5. Conclusions

In this study, we investigated a deep learning algorithm for the temperature structure inversion of mesoscale eddies in the South China Sea. The algorithm explores the influence of the SSH and SST on the temperature structure inversion of mesoscale eddies. It also uses different data fusion strategies, namely the inversion effects of single-stream and dual-stream neural networks. The effectiveness of the Dual_EddyNet algorithm proposed in this study was verified.

The model has a dual-stream structure, which includes a data fusion module to explore the correlation between sea surface parameters and achieve data fusion. It also contains a Triplet attention module, which performs dimension swapping, captures essential information about eddies, and improves the model's accuracy. The main contributions of this study are as follows: (1) Construction of a dataset for the temperature structure of mesoscale eddies in the South China Sea. The disadvantages of an uneven distribution, a low spatial resolution, and incomplete coverage of Argo data are compensated for through reanalysis of the data. (2) The proposal of a data-driven model (Dual_EddyNet) for the temperature structure inversion of mesoscale eddies, achieving inversion of the temperature structure between 0 and 1000 m in the South China Sea. (3) The effectiveness of the dual-stream model (in contrast to the conventional single-stream model structure) is verified through experimental comparisons. The proposed model (Dual_EddyNet) demonstrates a good accuracy in the temperature structure inversion of mesoscale eddies in the South China Sea. This method is of great significance for improving the accuracy of three-dimensional temperature structure prediction for mesoscale eddies. This method has the advantage of being lightweight and can be easily deployed on mobile system platforms. At the same time, it can provide a data reference for assimilations, numerical simulations, and other methods.

However, parameters such as sea surface wind fields and water currents influence mesoscale eddies. The unreliable eddy detection of the AVISO/CMEMS gridded products [39] is not considered in the dataset used in this study. Therefore, future work will further optimize this dataset and consider the impact of multi-source parameters on the inversion of mesoscale eddy fields. The inversion performance under different seasonal conditions will also be considered to further understand their effects on applicability and performance. Valuable directions for future work are comparative analyses and research on dynamic methods such as Surface Quasi-Geostrophic (SQG) methods, as well as the fusion of deep learning and dynamic-based methods [40].

Author Contributions: Conceptualization, J.H. and J.Y.; methodology, J.H. and J.Y.; validation, J.H., L.G. and G.L.; data curation, L.G. and W.C.; writing—original draft preparation, J.H.; writing—review and editing, J.H., J.Y. and J.Z.; visualization, L.G. and G.L.; supervision J.Z., J.W. and W.C. All authors have read and agreed to the published version of the manuscript.

Funding: This study is funded by National Natural Science Foundation of China No. 62231028 and No. 61931025.

Institutional Review Board Statement: Not applicable.

Informed Consent Statement: Informed consent was obtained from all subjects involved in the study.

Data Availability Statement: The original contributions presented in the study are included in the article. Further inquiries can be directed to the author.

Acknowledgments: The authors thank AVISO and CMEMS for providing satellite remote sensing data for free on their websites. We are grateful to anonymous referees and the editor who provided valuable comments improving the manuscript.

Conflicts of Interest: The authors declare no conflicts of interest.

References

1. Manso-Narvarte, I.; Rubio, A.; Jordà, G.; Carpenter, J.; Merckelbach, L.; Caballero, A. Three-Dimensional Characterization of a Coastal Mode-Water Eddy from Multiplatform Observations and a Data Reconstruction Method. *Remote Sens.* **2021**, *13*, 674. [[CrossRef](#)]
2. Moschos, E.; Barboni, A.; Stegner, A. Why do inverse eddy surface temperature anomalies emerge? The case of the Mediterranean Sea. *Remote Sens.* **2022**, *14*, 3807. [[CrossRef](#)]
3. Frenger, I.; Gruber, N.; Knutti, R.; Münnich, M. Imprint of Southern Ocean eddies on winds, clouds and rainfall. *Nat. Geosci.* **2013**, *6*, 608–612. [[CrossRef](#)]
4. Chelton, D.B.; Schlax, M.G.; Samelson, R.M.; de Szoeke, R.A. Global observations of large oceanic eddies. *Geophys. Res. Lett.* **2007**, *34*, L15606. [[CrossRef](#)]
5. Gaube, P.; Chelton, D.B.; Samelson, R.M.; Schlax, M.G.; O'Neill, L.W. Satellite observations of mesoscale eddy-induced Ekman pumping. *J. Phys. Oceanogr.* **2015**, *45*, 104–132. [[CrossRef](#)]
6. Feng, P.; Fu, Z.; Hu, L.; Wu, S.; Wang, Y.; Zhang, F. 3D-EddyNet: A Novel Approach for Identifying Three-Dimensional Morphological Features of Mesoscale Eddies in the Ocean. *J. Mar. Sci. Eng.* **2023**, *11*, 1779. [[CrossRef](#)]
7. Gaube, P.; Chelton, D.B.; Strutton, P.G.; Behrenfeld, M.J. Satellite observations of chlorophyll, phytoplankton biomass, and Ekman pumping in nonlinear mesoscale eddies. *J. Geophys. Res. Oceans* **2013**, *118*, 6349–6370. [[CrossRef](#)]
8. McGillicuddy Jr, D.J.; Robinson, A.; Siegel, D.; Jannasch, H.; Johnson, R.; Dickey, T.; McNeil, J.; Michaels, A.; Knap, A. Influence of mesoscale eddies on new production in the Sargasso Sea. *Nature* **1998**, *394*, 263–266. [[CrossRef](#)]
9. Hu, J.; Gan, J.; Sun, Z.; Zhu, J.; Dai, M. Observed three-dimensional structure of a cold eddy in the southwestern South China Sea. *J. Geophys. Res. Oceans* **2011**, *116*, C05016. [[CrossRef](#)]
10. Dong, C.; Lin, X.; Liu, Y.; Nencioli, F.; Chao, Y.; Guan, Y.; Chen, D.; Dickey, T.; McWilliams, J.C. Three-dimensional oceanic eddy analysis in the Southern California Bight from a numerical product. *J. Geophys. Res. Oceans* **2012**, *117*, C00H14. [[CrossRef](#)]
11. Jeong, Y.; Hwang, J.; Park, J.; Jang, C.J.; Jo, Y.-H. Reconstructed 3-D ocean temperature derived from remotely sensed sea surface measurements for mixed layer depth analysis. *Remote Sens.* **2019**, *11*, 3018. [[CrossRef](#)]
12. Ali, M.; Swain, D.; Weller, R. Estimation of ocean subsurface thermal structure from surface parameters: A neural network approach. *Geophys. Res. Lett.* **2004**, *31*, L20308. [[CrossRef](#)]
13. Ali, M.; Jagadeesh, P.; Lin, I.-I.; Hsu, J.-Y. A neural network approach to estimate tropical cyclone heat potential in the Indian Ocean. *IEEE Geosci. Remote Sens. Lett.* **2012**, *9*, 1114–1117. [[CrossRef](#)]
14. Su, H.; Wu, X.; Yan, X.-H.; Kidwell, A. Estimation of subsurface temperature anomaly in the Indian Ocean during recent global surface warming hiatus from satellite measurements: A support vector machine approach. *Remote Sens. Environ.* **2015**, *160*, 63–71. [[CrossRef](#)]
15. Su, H.; Li, W.; Yan, X.H. Retrieving temperature anomaly in the global subsurface and deeper ocean from satellite observations. *J. Geophys. Res. Oceans* **2018**, *123*, 399–410. [[CrossRef](#)]
16. Han, M.; Feng, Y.; Zhao, X.; Sun, C.; Hong, F.; Liu, C. A convolutional neural network using surface data to predict subsurface temperatures in the Pacific Ocean. *IEEE Access* **2019**, *7*, 172816–172829. [[CrossRef](#)]
17. Cosne, G.; Maze, G.; Tandeo, P. Coupling oceanic observation systems to study mesoscale ocean dynamics. *arXiv* **2019**, arXiv:1910.08573.
18. Chen, J.; Gong, X.; Guo, X.; Xing, X.; Lu, K.; Gao, H.; Gong, X. Improved Perceptron of Subsurface Chlorophyll Maxima by a Deep Neural Network: A Case Study with BGC-Argo Float Data in the Northwestern Pacific Ocean. *Remote Sens.* **2022**, *14*, 632. [[CrossRef](#)]
19. Yu, C.; Wang, J.; Peng, C.; Gao, C.; Yu, G.; Sang, N. Bisenet: Bilateral segmentation network for real-time semantic segmentation. In Proceedings of the European Conference on Computer Vision (ECCV), Munich, Germany, 8–14 September 2018; pp. 325–341.
20. Xie, H.; Xu, Q.; Cheng, Y.; Yin, X.; Fan, K. Reconstructing three-dimensional salinity field of the South China Sea from satellite observations. *Front. Mar. Sci.* **2023**, *10*, 1168486. [[CrossRef](#)]
21. Meng, L.; Yan, C.; Zhuang, W.; Zhang, W.; Yan, X.H. Reconstruction of Three-Dimensional Temperature and Salinity Fields From Satellite Observations. *J. Geophys. Res. Oceans* **2021**, *126*, e2021JC017605. [[CrossRef](#)]
22. Guinehut, S.; Dhomps, A.-L.; Larnicol, G.; Le Traon, P.-Y. High resolution 3-D temperature and salinity fields derived from in situ and satellite observations. *Ocean Sci.* **2012**, *8*, 845–857. [[CrossRef](#)]
23. Lin, X.; Qiu, Y.; Ni, X.; Lin, W.; Aung, C. Three-Dimensional Climatological Structures of the Arabian Sea Eddies and Eddy-Induced Flux. *J. Ocean Univ. China* **2023**, *22*, 874–885. [[CrossRef](#)]
24. Zhang, Z.; Tian, J.; Qiu, B.; Zhao, W.; Chang, P.; Wu, D.; Wan, X. Observed 3D structure, generation, and dissipation of oceanic mesoscale eddies in the South China Sea. *Sci. Rep.* **2016**, *6*, 24349. [[CrossRef](#)] [[PubMed](#)]
25. Jin, Q.; Tian, Y.; Sang, Q.; Liu, S.; Yu, J.; Wang, X. A deep learning model for joint prediction of three-dimensional ocean temperature, salinity and flow fields. In Proceedings of the 2021 6th International Conference on Automation, Control and Robotics Engineering (CACRE), Dalian, China, 15–17 July 2021; pp. 573–577.
26. Buongiorno Nardelli, B. A deep learning network to retrieve ocean hydrographic profiles from combined satellite and in situ measurements. *Remote Sens.* **2020**, *12*, 3151. [[CrossRef](#)]
27. Chelton, D.B.; Schlax, M.G.; Samelson, R.M. Global observations of nonlinear mesoscale eddies. *Prog. Oceanogr.* **2011**, *91*, 167–216. [[CrossRef](#)]

28. Chelton, D.B.; Gaube, P.; Schlax, M.G.; Early, J.J.; Samelson, R.M. The influence of nonlinear mesoscale eddies on near-surface oceanic chlorophyll. *Science* **2011**, *334*, 328–332. [[CrossRef](#)]
29. Pegliasco, C.; Busché, C.; Faugère, Y. Mesoscale Eddy Trajectory Atlas META3.2 Delayed-Time All Satellites. CNES 2022. Available online: <https://www.aviso.altimetry.fr/en/data/products/value-added-products/global-mesoscale-eddy-trajectory-product/meta3-2-dt.html> (accessed on 3 March 2024). [[CrossRef](#)]
30. Wang, Y.; Li, C.; Liu, Q. Observation of an anti-cyclonic mesoscale eddy in the subtropical northwestern Pacific Ocean from altimetry and Argo profiling floats. *Acta Oceanol. Sin.* **2020**, *39*, 79–90. [[CrossRef](#)]
31. Ni, Q.; Zhai, X.; LaCasce, J.; Chen, D.; Marshall, D. Full-depth eddy kinetic energy in the global ocean estimated from altimeter and Argo observations. *Geophys. Res. Lett.* **2023**, *50*, e2023GL103114. [[CrossRef](#)]
32. LeCun, Y.; Boser, B.; Denker, J.S.; Henderson, D.; Howard, R.E.; Hubbard, W.; Jackel, L.D. Backpropagation applied to handwritten zip code recognition. *Neural Comput.* **1989**, *1*, 541–551. [[CrossRef](#)]
33. Krizhevsky, A.; Sutskever, I.; Hinton, G.E. ImageNet classification with deep convolutional neural networks. *Commun. ACM* **2017**, *60*, 84–90. [[CrossRef](#)]
34. Simonyan, K.; Zisserman, A. Very deep convolutional networks for large-scale image recognition. *arXiv* **2014**, arXiv:1409.1556.
35. Ronneberger, O.; Fischer, P.; Brox, T. U-net: Convolutional networks for biomedical image segmentation. In Proceedings of the 18th International Conference on Medical Image Computing and Computer-Assisted Intervention–MICCAI 2015, Munich, Germany, 5–9 October 2015; pp. 234–241.
36. Liu, X.; Gao, Z.; Hou, F.; Sun, J. Learning the Spatiotemporal Evolution Law of Wave Field Based on Convolutional Neural Network. *J. Ocean Univ. China* **2022**, *21*, 1109–1117. [[CrossRef](#)]
37. Woo, S.; Park, J.; Lee, J.Y.; Kweon, I.S. Cbam: Convolutional block attention module. In Proceedings of the European Conference on Computer Vision (ECCV), Munich, Germany, 8–14 September 2018; pp. 3–19.
38. Misra, D.; Nalamada, T.; Arasanipalai, A.U.; Hou, Q. Rotate to attend: Convolutional triplet attention module. In Proceedings of the IEEE/CVF Winter Conference on Applications of Computer Vision, Virtual, 5–9 January 2021; pp. 3139–3148.
39. Stegner, A.; Le Vu, B.; Dumas, F.; Ghannami, M.A.; Nicolle, A.; Durand, C.; Faugere, Y. Cyclone-anticyclone asymmetry of eddy detection on gridded altimetry product in the Mediterranean Sea. *J. Geophys. Res. Oceans* **2021**, *126*, e2021JC017475. [[CrossRef](#)]
40. Chen, Y.; Liu, L.; Yuan, C.; Sun, X.; Chen, X.; Wei, Z.; Gao, Z. Physics-informed deep operator learning based on reduced-order modeling for retrieving the ocean interior density from the surface. *J. Geophys. Res. Oceans* **2024**, *129*, e2023JC019941. [[CrossRef](#)]

Disclaimer/Publisher’s Note: The statements, opinions and data contained in all publications are solely those of the individual author(s) and contributor(s) and not of MDPI and/or the editor(s). MDPI and/or the editor(s) disclaim responsibility for any injury to people or property resulting from any ideas, methods, instructions or products referred to in the content.